Volume 5
Number 4
April 2025
Pages 409–540

Environmental Science
Atmospheres

rsc.li/esatmospheres

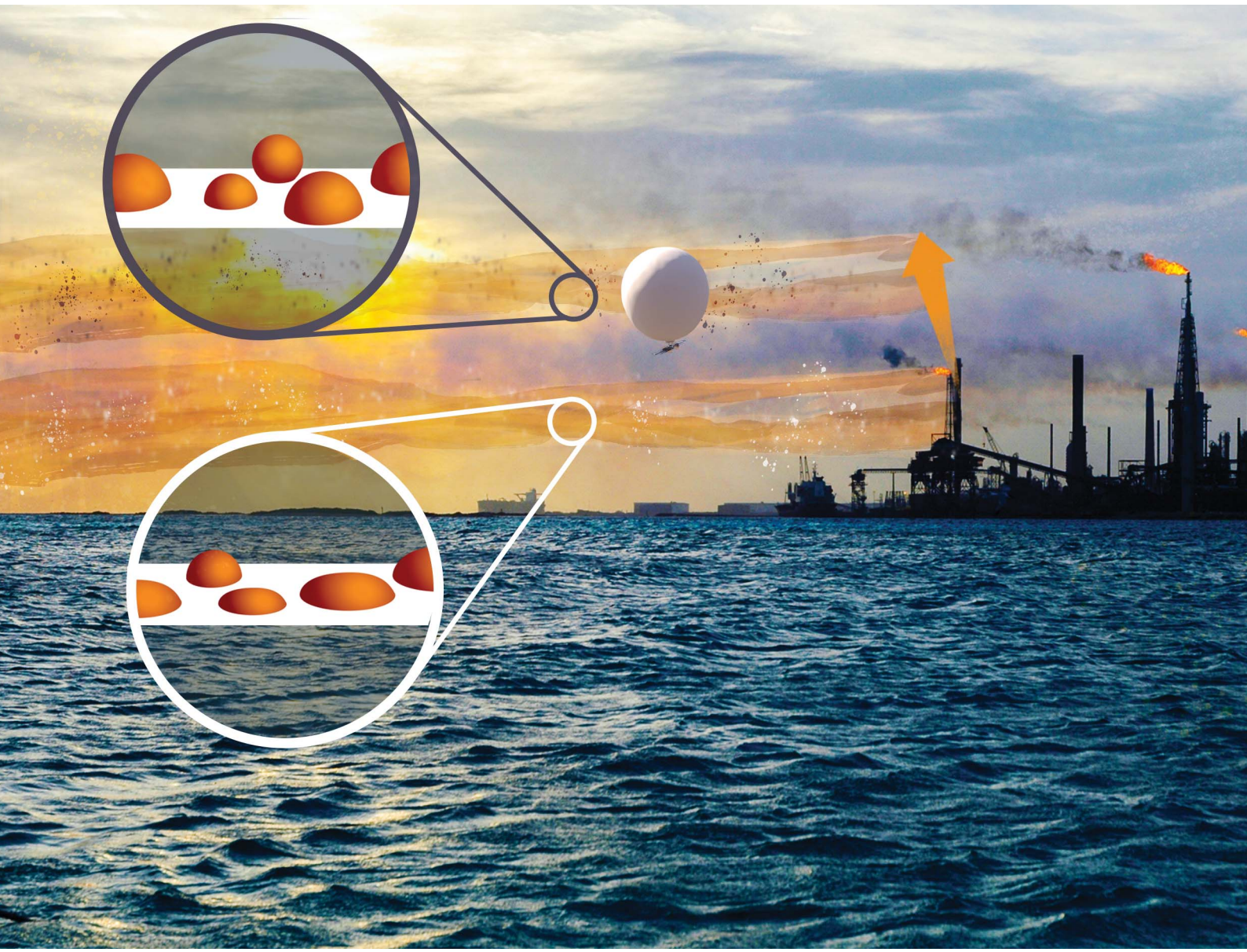

ISSN 2634-3606

ROYAL SOCIETY OF CHEMISTRY

PAPER
Swarup China *et al.*
Vertical gradient in atmospheric particle phase state: a case study over the alaskan arctic oil fields

Environmental Science: Atmospheres

ROYAL SOCIETY OF CHEMISTRY

PAPER

View Article Online
View Journal | View Issue

Cite this: *Environ. Sci.: Atmos.*, 2025, **5**, 415

Vertical gradient in atmospheric particle phase state: a case study over the alaskan arctic oil fields†

Nurun Nahar Lata, [a] Zezhen Cheng, [a] Darielle Dexheimer, [b] Susan Mathai, [ac] Matthew A. Marcus, [d] Kerri A. Pratt, [e] Theva Thevuthasan, [a] Fan Mei [f] and Swarup China *[a]

The phase state of atmospheric particles impacts atmospheric processes like heterogeneous reactions, cloud droplet activation, and ice nucleation, influencing Earth's climate. Factors like chemical composition, temperature, and relative humidity govern particle phase states. The Arctic atmosphere is stratified, with varying particle compositions, but vertical profiles of submicron phase states remain poorly understood due to limited aloft measurements. To address this, particle samples were collected *via* a tethered balloon system (TBS) at the U.S. Department of Energy Atmospheric Radiation Measurement Program's facility at Oliktok Point, Alaska, on November 19, 2020. Using an environmental scanning electron microscope with a tilted Peltier stage to simulate atmospheric conditions, we probed particle phase states, observing near-spherical, dome-like, and flat shapes upon substrate impact. Particles at an altitude of 300 m contained similar, high fractions of viscous particles (79 ± 9%) compared to ground-level (74 ± 5%). Chemical characterization revealed that carbonaceous-rich and carbonaceous sulfate-rich particles dominate ground-level samples, while 300 m samples included more carbonaceous-rich and carbonaceous-coated dust particles. STXM-NEXAFS further highlighted differences in particle mixing states, with a higher abundance of organic and mixed organic–inorganic particles at both altitudes. Integrating chemical composition and phase state measurements demonstrated that carbonaceous-rich and organic-dominated particles exhibited higher viscosities, while inorganic-rich particles displayed lower viscosities. This finding establishes an association between composition and phase state, offering critical insights into the vertical stratification of Arctic particles.

Received 22nd November 2024
Accepted 19th February 2025

DOI: 10.1039/d4ea00150h

rsc.li/esatmospheres

Environmental significance

Understanding the vertical gradient of particle phase states in the Arctic atmosphere, especially in areas influenced by anthropogenic emissions, is essential for predicting climate-related processes. The Alaskan Arctic, with its complex atmospheric composition shaped by natural and industrial activities, presents unique challenges in aerosol phase state characterization. This study highlights that submicron-size particles at different altitudes above Arctic oil fields vary in chemical composition but variation in viscosity is not significant. These findings highlight the importance of including altitude-specific phase states in climate models to enhance predictions of cloud dynamics and precipitation in the Arctic, contributing to a better understanding of global climate impacts.

1 Introduction

The present knowledge regarding the influence of atmospheric particles on climate is still insufficient. This state is attributed, in part, to the fact that atmospheric particles demonstrate a wide spectrum of viscosities, which makes it challenging to fully comprehend their effects.[1] The phase state of aerosol particles, which refers to the physical form of aerosol particles (solid and liquid), can have important implications for atmospheric processes and human health.[1] In the atmosphere, aerosol particles can act as cloud condensation nuclei (CCN) or ice nuclei (IN), both of which influence cloud properties and precipitation.[2,3] The phase state of aerosol particles can affect their ability to act as CCN or IN,[4–10] as well as their optical properties.[11] Particle phase state also can affect reactivity and heterogeneous reaction rates,[12,13] pollutant transport (*e.g.*, polycyclic aromatic hydrocarbons (PAHs)),[14,15] and growth rate during gas–particle partitioning.[16] For example, solid particles promote ice nucleation *via* the deposition mechanism and can

[a]*Environmental Molecular Sciences Laboratory, Pacific Northwest National Laboratory, Richland, WA 99354, USA. E-mail: Swarup.China@pnnl.gov; Tel: +1 509 371-7329*

[b]*Sandia National Laboratory, Albuquerque, NM 87123, USA*

[c]*Michigan Technological University, Houghton, MI, 49931, USA*

[d]*Advanced Light Source, Lawrence Berkeley Lab, Berkeley, California 94720, USA*

[e]*Department of Chemistry and Department of Earth and Environmental Science, University of Michigan, Ann Arbor, MI 48109, USA*

[f]*Atmospheric, Climate, & Earth Sciences Division, Pacific Northwest National Laboratory, Richland, WA 99352, USA*

† Electronic supplementary information (ESI) available. See DOI: https://doi.org/10.1039/d4ea00150h

trigger the formation of cirrus clouds, which can have significant impacts on the Earth's energy balance.[1,7,9,10]

The phase state of aerosol particles can be influenced by several factors such as emission source, formation mechanism, chemical composition, size, mixing state, and ambient conditions (relative humidity [RH] and temperature).[17–23] RH changes can lead to the formation of droplets or crystalline structures, while temperature changes can induce phase transitions such as sublimation, melting, or evaporation.[18] The chemical composition of aerosol particles also can play a crucial role in determining their phase state, with water-soluble ions, such as sulfate, nitrate, and chloride, affecting aerosol–water interactions.[24,25] Therefore, a comprehensive understanding of the phase state of aerosol particles is crucial for predicting their impacts on the Earth's atmosphere.

Arctic aerosols exhibit a pronounced seasonal cycle,[26,27] with elevated mass loading during winter and spring due to long-range transport of pollutants from mid-latitudes and low-latitudes.[28–30] In contrast, summer sees lower mass loading primarily from local biogenic sources and sea spray particles, occasionally augmented by transport of particles from low-latitude wildfires.[31–33] The U.S. Department of Energy (DOE) Atmospheric Radiation Measurement (ARM) established a mobile research facility at Oliktok Point, Alaska, which is located on the north-west edge of oil extraction activities on the North Slope of Alaska and northwest of Prudhoe Bay.[34] Natural and anthropogenic processes, including local oil field extraction emissions, burning natural gas and diesel fuel, venting/flaring, *etc.*, contribute to Arctic aerosol population.[35] An earlier study found heightened aerosols and trace gases in Alaskan Arctic summertime air, attributed to local oil extraction, 2015 wildfires, and long-range transport, surpassing previous Arctic haze measurements, with potential broader impacts despite episodic or localized origins.[36] Another study at the same site found that the presence of local industrial pollutants decreases cloud droplet radii from 12.2 to 9.4 μm, resulting in lower levels of drizzle and precipitation.[37] Several studies revealed the chemical composition of the oilfield aerosol particles at Oliktok Point and downwind at Utqiaġvik, Alaska.[38–44] None of these prior studies reported the viscosity and phase condition of particles at this site.

Numerous investigations have focused on exploring the viscosity and phase condition of submicron-sized particles that are pertinent to the atmosphere.[13,45–51] However, only a small number of these studies have presented field measurements regarding the phase state of ambient particles.[8,19,49,52–58] Limitations of measurement techniques have resulted in a data gap. For example, online measurements of phase state are challenging because of the low concentrations of particles in remote locations. Some offline techniques, such as the poke-flow technique, are not be suitable for phase-state measurements of submicron size atmospheric particles.[56,58] Additionally, research concerning the aerosol particle phase state above-ground level is limited.[8,58] Moreover, the phases of the aerosol particles found at ground level can be different than the phase of the particles found aloft due to variations in temperature and RH at different altitudes. Recent studies have highlighted the complex internal mixing states of atmospheric particles, particularly the phase separation between organic components and inorganic salts, which can significantly influence aerosol–cloud interactions and ice nucleation processes.[59] Understanding these phase relationships is essential for accurately assessing the climate impacts of aerosols, especially in cold and remote environments.

A recent study at Oliktok Point showed the vertical variability of size-resolved aerosol composition using a tethered balloon system in Oliktok Point, Alaska.[60] The study revealed distinct characteristics in two case studies (*i.e.*, background aerosol and polluted conditions), with findings suggesting cloud processing of aerosols and the potential role of carbonaceous particles in modulating Arctic cloud properties.[60] A few modeling studies have simulated the vertical variability of the aerosol particle phase state over eastern and western USA[61] and Amazonia rainforest[62] however, no experimental study has been performed to examine the vertical variation of aerosol particle phase state at Oliktok Point Alaska. These challenges can be addressed by collecting atmospheric particles on substrates at various altitudes and analyzing their phase states offline, while mimicking the atmospheric conditions of temperature and RH.[56] One such analysis involves the use of tilted scanning electron microscopy (SEM) imaging to identify the phase states of particles based on the shapes they acquire when they impact the substrate.[1,56,63] By using this approach, we have developed an analytical platform that leverages tilted environmental scanning electron microscope (ESEM) imaging to directly observe and assess the phase states of particles by analyzing their shape deformation on the substrate. This study focuses on a case study evaluation of the vertical variation of aerosol particle phase state over the Alaskan Arctic oil fields and links the information acquired to chemical composition, mixing state, and environmental conditions.

2 Methods

2.1 Particle sampling *via* tethered balloon system

A tethered balloon system (TBS) flight was conducted on November 19, 2020, at Oliktok Point, Alaska (70.51°N, 149.86° W, 2 m above mean sea level (a.m.s.l.)), at the Department of Energy (DOE) Atmospheric Radiation Measurement (ARM) Mobile Facility (AMF3) from 00:55 UTC to 07:43 UTC to probe the vertical profile of aerosol particle phase state. Aerosol particles were collected at both ground level and aloft for the offline physicochemical analysis onto transmission electron microscopy (TEM) grid substrates (carbon Type-B, Ted Pella Inc.). Sampling at ground level was performed using a Sioutas Personal Cascade Impactor, SKC, Inc. For sampling aloft, a size and time resolved aerosol collector (STAC) was deployed with each TBS flight.[64] The STAC particle sampling was done at multiple different altitudes above ground level (100–300 m) (Table S1†) to probe variations in aerosol particle phase state *versus* altitude. Field-collected particle samples were stored in a dedicated TEM-grid box wrapped with aluminum foil and kept in zip-lock bags to avoid light and air exposure.[65] However, we cannot rule out the possibility that some modifications may

have occurred between sampling and analysis. This is a drawback of offline field sample analysis. For both impactors, we focused on the analysis particles collected on stage *D*, which has 50% cut-off size 0.25 and 0.12 μm for Sioutas and STAC impactors, respectively, due to the poor loading on other stages. We note that the SEM-derived 2D projected area–equivalent diameter may differ from the aerodynamic diameter used in the impactor, as the aerodynamic diameter accounts for particle shape and density, while the SEM measurement reflects only the geometric size. Bouncing of particles from higher stage to lower stage can happen as well based on the viscosity of the particles.

The TBS sampling was performed *via* loitered ascending and descending flights. For the TBS flights, we deployed an iMet to probe ambient conditions (temperature and RH)[66] and one portable optical particle spectrometer (POPS) to obtain size distributions within a size range of 0.13–3 μm.[67] Particle samples were collected at multiple altitudes while the TBS remained stationary, loitering for approximately 20 minutes at each level. This approach allowed to investigate vertically resolved aerosol properties under specific atmospheric conditions. However, given the dynamic nature of the atmosphere, the representativeness of the data may still be influenced by temporal and spatial variability, including changes in meteorological conditions, air mass characteristics, and localized emissions during the sampling period. While this study provides valuable insights into aerosol phase state variability, it is inherently a case study. Future investigations incorporating repeated flights under diverse atmospheric conditions and extended timeframes will be essential for developing a more comprehensive understanding of vertical aerosol distribution and variability.

2.2 Micro-spectroscopic and chemical imaging of particles

We used multi-modal micro-spectroscopy techniques to characterize the vertically resolved atmospheric particles. We used a computer-controlled SEM (Thermo Fisher Scientific Quanta environmental SEM) with energy-dispersive X-ray spectroscopy (CCSEM-EDX), which allows for automated particle detection and acquisition of X-ray spectra, and measurement of particle size, morphology, and elemental composition (as atomic percentages) of thousands of individual particles.[68–70] For this study, a total of 6121 particles were analyzed across all samples (Table S2†). Based on the atomic percentage data, particles were then classified into eight classes using rule-based classification described in an earlier study.[8] We looked at individual particle carbon features with scanning transmission X-ray microscopy coupled with near-edge X-ray absorption and fine structure (STXM/NEXAFS) (beamline 5.3.2.2) at Lawrence Berkeley National Laboratory's Advanced Light Source (ALS). We collected both spectral "stack" and "map" data.[71] Data collected *via* STXM/NEXAFS were classified into different mixing state classes based on the distribution of different species, such as organic carbon (OC), elemental carbon mixed with OC (EC + OC), OC mixed with inorganics (IN + OC), inorganics (IN), and particles with OC, EC, and IN inclusions (OC + EC + IN).[71,72] Details of single particle analyses are discussed in the ESI.† It also is noteworthy that the characterizations of carbonaceous particles identified *via* (CCSEM/EDX) differ somewhat from OC particles as defined by STXM/NEXAFS. The CCSEX/EDX-derived carbonaceous class may contain other organic and inorganic carbon species, whereas STXM-derived OC is based on the height of the baseline-subtracted carboxylic acid peak.

2.3 Observation of phase state under atmospheric conditions

We used a tilted (60° tilt) Peltier stage fitted inside an ESEM (Quanta 3D, Thermo Fisher) chamber to probe the phase state of the particles.[56] To mimic atmospheric conditions, we used the mean temperature and RH value retrieved from iMet at each altitude (Table S3†) and set that for each sample. The operating temperature range of the Peltier stage is 263–303 K. To mimic the atmospheric RH for different samples, the chamber pressure is adjusted between 0.08 and 6.5 torr. A combination of Gaseous Secondary Electron Detector (GSED) and Scanning Transmission Electron Microscopy (STEM) detector was used to image the individual particles at controlled RHs from 0 to 100% with an uncertainty of ±1%. Atmospheric particles often are mixed with organic and inorganic constituents. The phase state obtained from this method provides the phase state of the whole individual particle. We acknowledge that one limitation of this method is evaporation of semi-volatile material under the ESEM mode where the pressure range is 0.08–6.5 torr; note, however, that this pressure is still very high compared to the high vacuum SEM mode where the chamber pressure remains at $\sim 2 \times 10^{-6}$ torr. It is important to consider that certain particle modifications may have occurred between the time of sampling and analysis. For example, suppose particles transition from solid-to-liquid state due to higher temperature during storage, compared to collection. In that case, they may not revert to the solid state due to surface tension, friction, and adhesion forces between the substrate and particle. However, if organic materials contain solid inorganic components such as dust, soot, or salt, the particle shape may become irregular and may not adhere to the aspect ratio threshold proposed for organic particles in the previous study.[56] Consequently, this study focuses solely on examining the phase states of organic particles that maintain a regular (*e.g.*, spherical, hemispherical, and ellipsoidal) shape. The collected SEM images were analyzed with ImageJ software to obtain the aspect ratio (*i.e.*, the ratio of particle height to width) of each particle which provides its phase state.[8,56,58,73] High-viscosity particles, resembling solids or semi-solids, upon impact with the substrate maintain aspect ratios between 1 and 0.54, while low-viscosity particles flatten, yielding aspect ratios <0.54.[56] We adopted the method described in a previous study to obtain corrected aspect ratios, which involves calculating tilted aspect ratios from tilted ESEM images.[56] This approach involves the computation of tilted aspect ratios from ESEM images captured at a tilt angle of 60°. Specifically, the tilted aspect ratio is determined as the ratio of the projection of the arc from the top to the base onto the horizontal plane to the projection of the base width onto the

horizontal plane. For solid spherical particles, tilted and corrected aspect ratios align, while semi-solid and liquid particles exhibit vertical distortion. In cases of exceedingly flat particles, which is indicative of a liquid state with significantly low viscosity, height represents the projection of the vertical diameter of the base onto the horizontal plane, leading to a tilted aspect ratio less than or equal to cos (tilt angle) (set at 0.5 in this study).

2.4 Backward air mass trajectory analysis

To understand the sources of air masses, 24 h NOAA Hybrid Single Particle Lagrangian Integrated Trajectory (HYSPLIT)[74] backward airmass trajectories were performed at model vertical velocity. Fig. S1† shows 24 hours HYSPLIT Back Trajectory analysis of the air masses during the sampling time on November 19, 2020. Fig. S1(a)† shows the air masses' source for ground particle sampling, while panel (b–e) show the air masses' source for aloft particle sampling. The analysis was performed using the GDAS (Global Data Assimilation System) meteorological dataset, with vertical motion calculated using model vertical velocity and a duration of 24 hours. The starting heights for aloft sampling were 100 m, 200 m, and 300 m AGL (above ground level). Image (f) shows the wind rose plot, indicating the wind speed distribution during the sampling period. Air masses for all the samples were transported from the south across tundra and the North Slope of Alaska oil fields. The aerosol particles originating from the oil fields significantly influence particle composition at the ARM Oliktok Point site.[44] For the ground sample, the air mass traveled near the surface (<500 m) before reaching the sampling location (Fig. S1(a)†). The air masses for the 100 m (ascending) and 300 m (ascending) flights traveled from the highest altitude (~1,500 m) before reaching the sampling location.

3 Result and discussion

3.1 Evolution of meteorological condition and direct measurement of particle phase state at conditions mimicking the atmosphere at various altitudes

Fig. 1(a) shows the TBS flight profile of the particle sampling. The aerosol particles were collected at multiple altitudes for ascending–loitering and descending–loitering flights.[60] The aerosol particles were collected at ground level, 100 m ascending–loitering, 200 m ascending–loitering, 300 m ascending–loitering, and 200 m descending–loitering. The RH and temperature profile of the TBS flight was retrieved from iMet. At 100 m altitude, the mean RH and temperature were 56 ± 1% and −1.9 ± 0.1 °C, respectively. For the 300 m altitude samples, the mean RH and temperature was 42 ± 2% and 0.9 ± 0.3 °C, respectively. Variations in temperature and RH can affect the physicochemical properties of an aerosol particle at that altitude.

Fig. S2† shows the particle concentration and size distribution obtained from POPS. The mean total particle concentration obtained from POPS (0.13–3 μm) varied across altitudes. The POPS values showed the highest mean total concentration (45 ± 6 # per cm^3) at low altitude (at 100 m). The mean total concentration at 200 m (both ascending and descending flights) was low (25 ± 2 # per cm^3) and similar at 300 m (27 ± 6 # per cm^3). Fig. S3† shows the 5 minutes mean of RH (left panel) and temperature (right panel). The shaded region indicates the sampling time span at each altitude. The standard deviation at each sampling altitude is minimal for RH and temperature. The RH was below saturation at all the altitudes. A temperature inversion was observed at 300 m. Previous studies have reported that frequent temperature inversions in the Arctic play a pivotal role in modulating aerosol dispersion, vertical radiative heating distribution, and the intricate dynamics of Arctic cloud and radiation processes.[75–77]

To understand atmospheric stability, we calculated the environmental lapse rate (ELR) at the altitudes where the particle samples were collected. The ELR was determined by measuring the change in temperature with altitude from available temperature and altitude data. If the ELR is less than the dry adiabatic lapse rate (DALR) of approximately 9.8 °C km^{-1}, the atmosphere is considered stable; otherwise, the atmosphere is considered to be unstable.[78] The estimated ELRs for the 100 m ascending, 200 m ascending, and 200 m descending flights were −9.2 °C km^{-1}, 5 °C km^{-1}, and −25 °C km^{-1}, respectively, all of which were less than 9.8 °C km^{-1}, thus indicating stable atmospheric layers, which inhibit vertical mixing and trap particles closer to the ground. In the case of the 300 m ascending flight (200–300 m), the ELR is 23 °C km^{-1} which is greater than the dry adiabatic lapse rate (9.8 °C km^{-1}), indicating an unstable atmospheric layer that can promote vertical mixing. The significant difference in the ELRs between ascending and descending flights may be attributed to potential meteorological shifts between the flight times, variations in local atmospheric phenomena, or differences in wind profiles that could affect temperature gradients.

The phase states of the aerosol particles at various altitudes were probed, mimicking during ESEM the ambient conditions during sample collection. Note that only organic particles with regular (*e.g.*, spherical, hemispherical, and ellipsoidal) shapes were probed. Representative ESEM images are shown in (Fig. 1(b)–(f)). To get a comprehensive idea of particle phase state, we measured the aspect ratio of the particles by taking the ratio of height-to-width of the particle from ESEM images using ImageJ software.[73] Fig. 1(g) shows the measured aspect ratios of the particles. The viscosity boundary is adopted from a previous study.[56] The high viscosity particles with solid or semi-solid-like consistencies when impacting a substrate tend to maintain a high aspect ratio of 1–0.54. On the other hand, low viscosity particles with liquid-like consistencies tend to become more oblate when impacting a substrate, resulting in lower aspect ratios (<0.54). We observed different distributions of aspect ratios for particles obtained at various altitudes. To assess the different aerosol particle phases present in each samples, we quantified the number fraction of the particles in each phase boundary[56] (Fig. 1(h)). The ground sample contains 74 ± 5% of high viscosity particles (semi-solid: 66 ± 5% and solid: 7 ± 3%) and 26 ± 5% low viscosity particles. Particles collected at 100 m showed a similar percentage (78 ± 4%) of high-viscosity

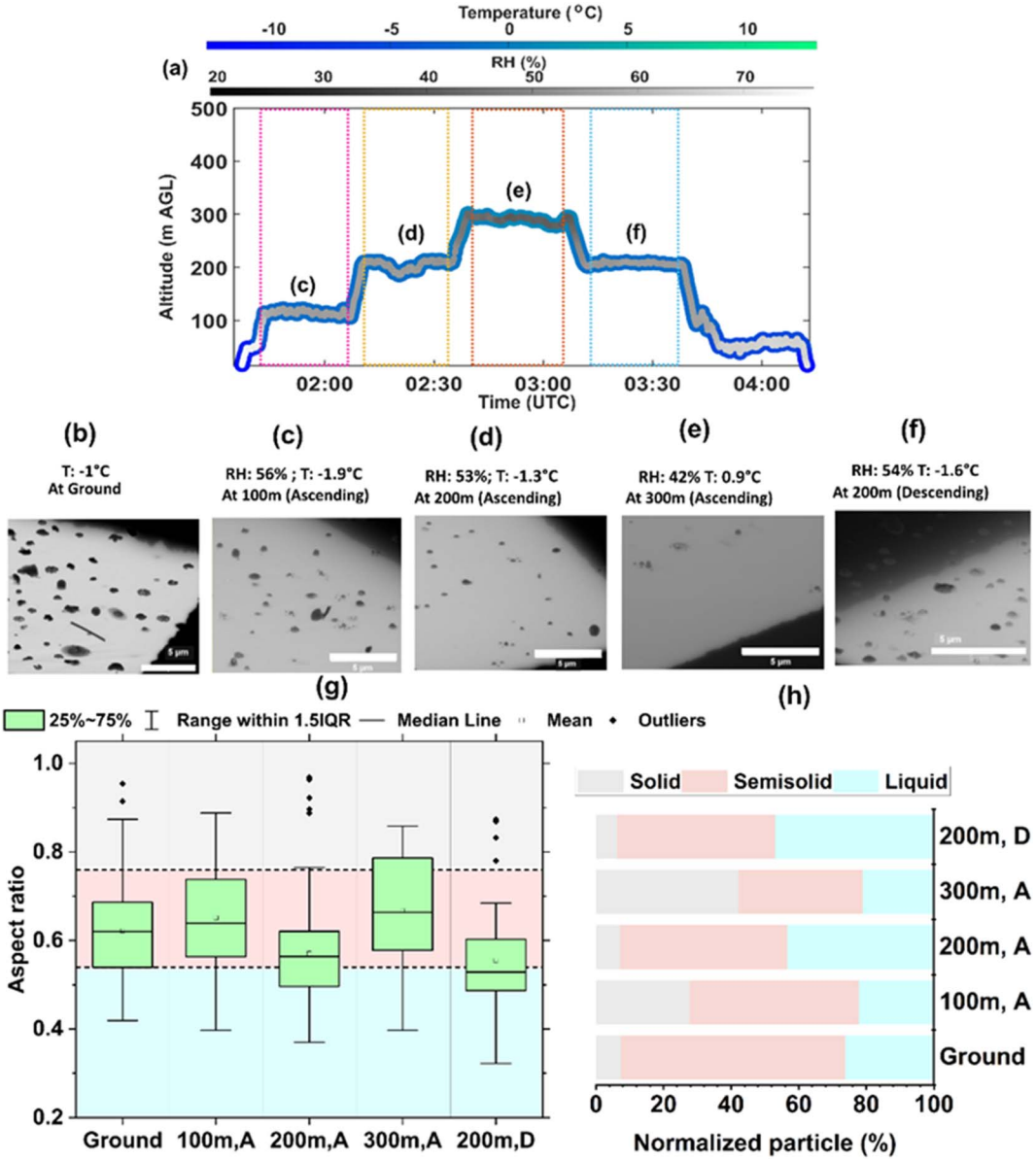

Fig. 1 (a) TBS flight profile (temperature and RH) of November 19, 2020, sampling. The aerosol particles were collected *via* loitering flight. The dotted region indicates the sampling period. Ambient aerosol particle samples were collected using the STAC platform at about 100 m (ascending), 200 m (ascending), 300 m (ascending) and 200 m (descending) above ground level. The color bars on the top represent RH and temperature. (b–f) Tilted ESEM images of the particles mimicking the atmospheric RH and temperature to reveal the phase state. (g) Distributions of aspect ratio of the particles at different altitudes. Here, the suffix '*A*' means ascending and '*D*' means descending. Total number of particles analyzed at the ground is 95, 100 m is 90, 200 m *A* is 97, 300 m is 19 and 200 m, *D* is 74. (h) Number fractions of solid, semi-solid, and liquid organic particles at different altitudes.

particles, but with different percentages of semi-solid (50 ± 5%) and solid (28 ± 5%) particles than those collected at ground level. Particles collected at 300 m contain a similar percentage (79 ± 9%) of high viscosity particles as both ground-level and 100 m, with a similar percentage of semi-solid (37 ± 11%) and solid (42 ± 11%) particles as at 100 m. In comparison, particles collected at 200 m ascending and descending sampling show a higher percentage of low viscosity (36–43%) particles than the other altitudes.

To evaluate the potential impact of phase-dependent particle bounce on our viscosity and composition measurements, we analyzed the relationship between particle aspect ratio and area–equivalent diameter (AED) across all sampled altitudes (Fig. S4†). Our data reveal a broad distribution of solid, semi-solid, and liquid particles across size ranges. This indicates that phase-dependent collection bias due to bounce is minimal. Additionally, it is important to recognize that the SEM-derived 2D projected area–equivalent diameters used in our analysis do not directly correspond to the aerodynamic diameters that govern particle collection in impactor stages. This difference limits the direct correlation between phase state and size-resolved collection behavior.

3.2 Evolution of chemical composition of particles as a function of altitude

Fig. 2(a)–(e) show the size resolved chemical composition of particles probed with CCSEM/EDX. A total of 6121 particles were characterized for this case study. The representative single-particle images and spectra are shown in Fig. S4.† The ground sample was mainly composed of carbonaceous-rich (71 ± 1%, by number) and carbonaceous-rich sulfate (20 ± 1%) particles, with minor contributions of Na-rich (sea salt), Na-rich sulfate (aged sea salt), and dust (Fig. 2(a)). The CCSEM/EDX size distribution in this sample is bimodal and wider than in the other samples. Particles in the <1 μm size range are dominated by carbonaceous-rich species, and >1 μm are dominated by carbonaceous-rich sulfate. The sample collected at 100 m is dominated by carbonaceous-rich (88 ± 1%) and Na-rich particles (8 ± 1%), with minor sulfate, Na-rich sulfate, and dust contributions (Fig. 2(b)). For this sample, the CCSEM size distribution is comparatively narrower than the ground sample. Particles in size bins <1.1 μm are dominated by carbonaceous, and >1.1 μm are dominated by Na-rich particles. The POPS size distribution is narrow during sampling at 100 m (Fig. S2†).

The particle population at 200 m altitude (ascending) was dominated by carbonaceous-rich (58 ± 1%, by number) and carbonaceous-rich sulfate (33 ± 1%) particles, with minor contribution of Na-rich (3.0 ± 0.5%), Na-rich sulfate (3 ± 1%) and dust (0.3 ± 0.2%) (Fig. 2(c)). For this sample, we observed a bimodality in size-distribution with a dominance of carbonaceous-rich at <0.5 μm and carbonaceous-rich sulfate at >0.5 μm. The highest altitude (300 m) particles were dominated by carbonaceous-rich (77 ± 2%) and carbonaceous-rich dust (15 ± 2%) particles with dust (6 ± 1%) and a very minor fraction of carbonaceous-rich sulfate (0.2 ± 0.2%) (Fig. 2(d)). In the case of this sample, Na-rich sulfate and sulfate-rich dust particles were absent. This sample shows the narrowest particle size distribution, where particle size bins <0.5 μm were dominated by carbonaceous and >0.5 μm were dominated by dust and coated dust. Aerosol particles at 200 m (descending) were dominated by carbonaceous-rich (45 ± 1%), carbonaceous-sulfate-rich (42 ± 1%), Na-rich (5 ± 1%), Na-rich sulfate (5 ± 1%), and a minor percentage of dust (1.0 ± 0.2%). The size distribution indicates a bimodality where particle size bins <0.3 μm are dominated with carbonaceous and >0.3 μm are dominated with sulfate (Fig. 2(e)). This sample contains the highest number fraction of

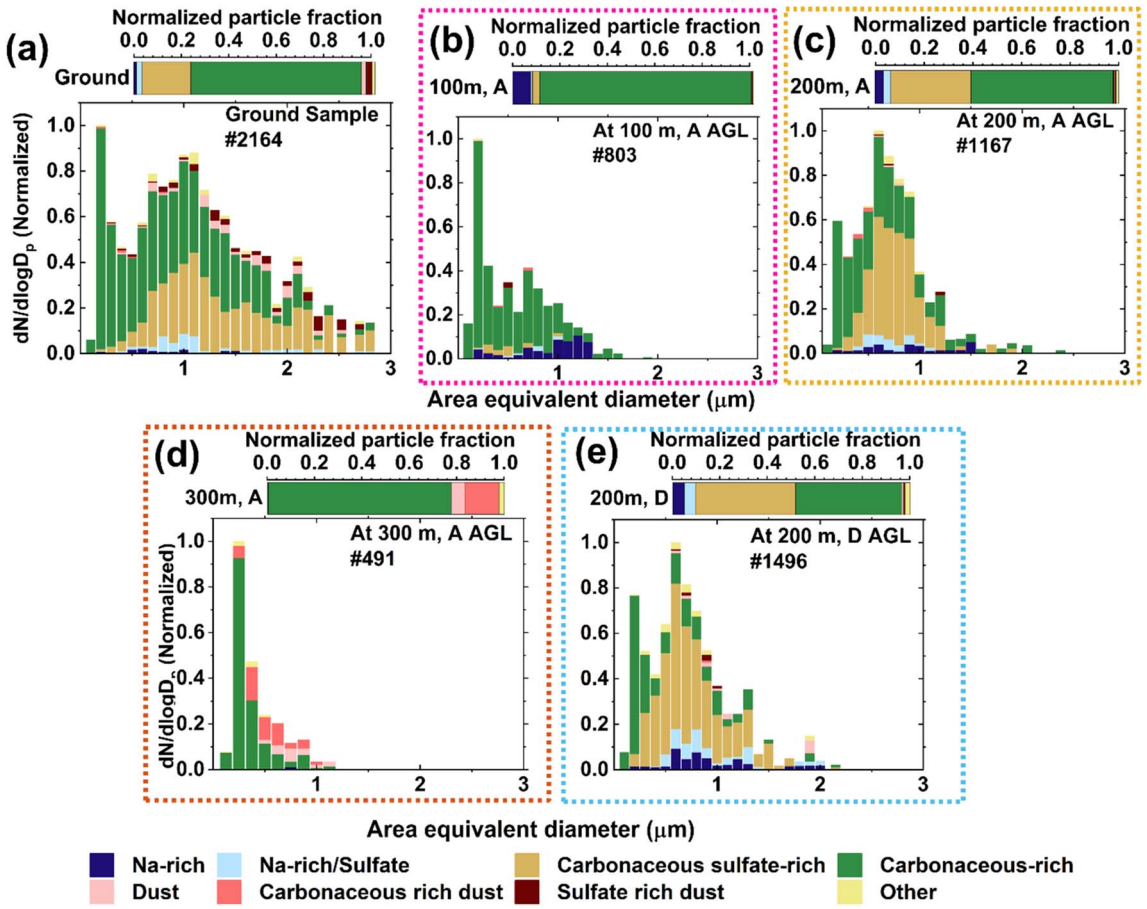

Fig. 2 (a) shows the CCSEM/EDX size distribution of the particles collected at ground level. Different colors indicate the identified particle classes within the sample. On top of each size-distribution plot, the normalized particle fraction of each of the classes is shown. (b–e) Show the size-resolved chemical composition of the mentioned altitudes, with *A* depicting ascending and *D* corresponding to descending. The (#) number inside each plot (a–e) indicates the total number of particles analyzed for each of the samples.

sulfate particles. A similarity in size-resolved chemical composition is observed for both samples collected at 200 m (ascending and descending flights). Overall, we observed a variation of size-resolved chemical composition, RH, and temperature at different altitudes, which indicates vertical stratification of the Arctic atmosphere.

Our findings align with earlier observations of high-viscosity particles, as demonstrated by a recent study reporting solid organic-coated ammonium sulfate particles collected during the Arctic summertime.[55] Chemical composition of the particles and ambient conditions might be responsible for the observed difference in phase states of particles at different altitudes. Previous studies have shown that the viscosity of a mixture containing both organic and inorganic components (*e.g.*, nitrate, sulfate, and sodium salt) tends to decrease as the proportion of inorganic content increases.[6,79–84] As the proportion of inorganic content rises, it effectively reduces the viscosity of the mixture. The carbonaceous sulfate-rich particles are hygroscopic and at elevated RH become more liquid-like. The reduction in viscosity is linked to the higher hygroscopic properties of the inorganic components, leading to an overall enhancement in the hygroscopicity of the internally mixed particles and transition to a semi-solid and liquid phase before reaching the deliquescence RH at 78%.

Building on this, we conducted a correlation analysis to further investigate the relationship between aerosol chemical composition and phase state under Arctic conditions, using aspect ratio. Correlation analysis (Fig. S6†) reveals that aspect ratio decreases with increasing Na-rich/sulfate and carbonaceous sulfate fractions. Higher sulfate fractions are associated with more liquid-like or semi-solid particles (aspect ratio < 0.77), suggesting that sulfates enhance water uptake or suppress crystallization. Similarly, an increase in carbonaceous sulfate fractions also leads to lower aspect ratios, indicating that carbonaceous sulfate aerosols remain in liquid or semi-solid states, consistent with their hygroscopic and low-viscosity behavior under Arctic conditions. These results establish an association between aerosol chemical composition and phase state, advancing our understanding of the phase state of Arctic aerosol.

3.3 Effect of chemical mixing state and organic volume fraction on phase state variability across altitude

A previous study shows that aerosol chemical mixing state affects particle viscosity.[83] We employed STXM/NEXAFS spectromicroscopy techniques to gain spatially resolved insights into carbon bonding speciation, allowing us to differentiate between EC and OC regions within individual particles, as detailed in an earlier study.[71] The STXM/NEXAFS mapping of carbon composition at the carbon K-edge reveals the three primary components based on spectral information:[71] IN (inorganic), OC (organic carbon), and EC (elemental carbon). In each pixel within an individual particle, there exists a potential for singular or multiple components, resulting in possible overlap of these constituents. Consequently, these overlapping constituents were categorized into five typical particle classes, discerned by the internal mixing of OC, EC, and IN components with an individual particle: (1) IN, (2) OC–EC–IN, (3) OC–EC, (4) OC–IN, and (5) OC. We can link the STXM/NEXAFS particle classes to the CCSEM/EDX particle classes. Class IN includes dust and Na-rich particles; classes OC and OC–EC include some portions of the carbonaceous-rich particles, and classes OC–IN and OC–EC–IN include carbonaceous-rich sulfate, Na-rich sulfate, and carbonaceous-coated dust particles.

Fig. 3 shows the vertically resolved chemical mixing state of the particles probed with STXM/NEXAFS. Most particles in the particle population are internally mixed with OC, EC, and IN. A previous study at this site found that plumes from oil and gas extraction contain soot internally mixed with sulfate and organic carbon with ammonium sulfate salts, while coastal sea spray aerosols are internally mixed with sulfate and nitrate from chemical processing.[44] For this study, samples collected at 300 m contain elevated number fractions of OC ($47 \pm 7\%$) and OC + EC ($20 \pm 6\%$). In comparison, there was a lower number fraction of solid-like particles at 100 m which was dominated by OC + IN ($79 \pm 3\%$, by number) particles. In this case, possibly the coating material plays a vital role in explaining the particle phase state. The particles collected at 300 m showed the highest fraction of OC and OC + EC and were dominated by carbonaceous-rich and solid-like particles. An earlier study reported that particles from central Amazonia consisting of biogenic organics, sulfate, and black carbon revealed a high viscosity state at high RH during the influence of urban pollution and biomass burning.[53] We want to note that lower particle counts at 300 meters AGL can be attributed to a combination of meteorological[77] and lower particle concentration. The unstable atmospheric layer identified by the elevated environmental lapse rate (23 °C km^{-1}) indicates enhanced vertical mixing, which likely dispersed aerosols over a larger vertical range, thereby reducing localized concentrations at this altitude.[77]

Local oil and gas extraction activities, particularly near the Prudhoe Bay region, are significant sources of OC and OC + EC particles in the Arctic.[38,44,85] Studies have shown that these emissions, primarily from combustion processes, add organic and elemental carbon to the atmosphere, impacting the Arctic aerosol composition to OC and OC + EC particle emissions in the Alaskan Arctic. The higher number fraction of OC and OC + EC particles from this study could originate from local anthropogenic emissions. Previous studies found that some carbonaceous particles are amorphous, round, non-crystalline, and solid[86,87] and originated from biomass burning.[86,87] Numerous studies have shown that certain organic aerosol particles can persist as solid glasses or semi-solids at lower temperatures due to the reduced diffusion rate of water at colder conditions.[88–90] This possibly explains why we observed more solid and semi-solid particles in the sample containing high number fraction of OC ($47 \pm 7\%$) and OC + EC ($20 \pm 6\%$) at 300 m. Low temperatures (0.9 to −1.9 °C) in the Arctic atmosphere during early winter can contribute to the existence of OC particles in solid and semi-solid phase states. We also retrieved the spectral information from the STXM-NEXAFS data collected for aloft samples. Fig. S5† shows the average of 19 particle spectra collected for aloft samples (100–300 m). From this figure, we can

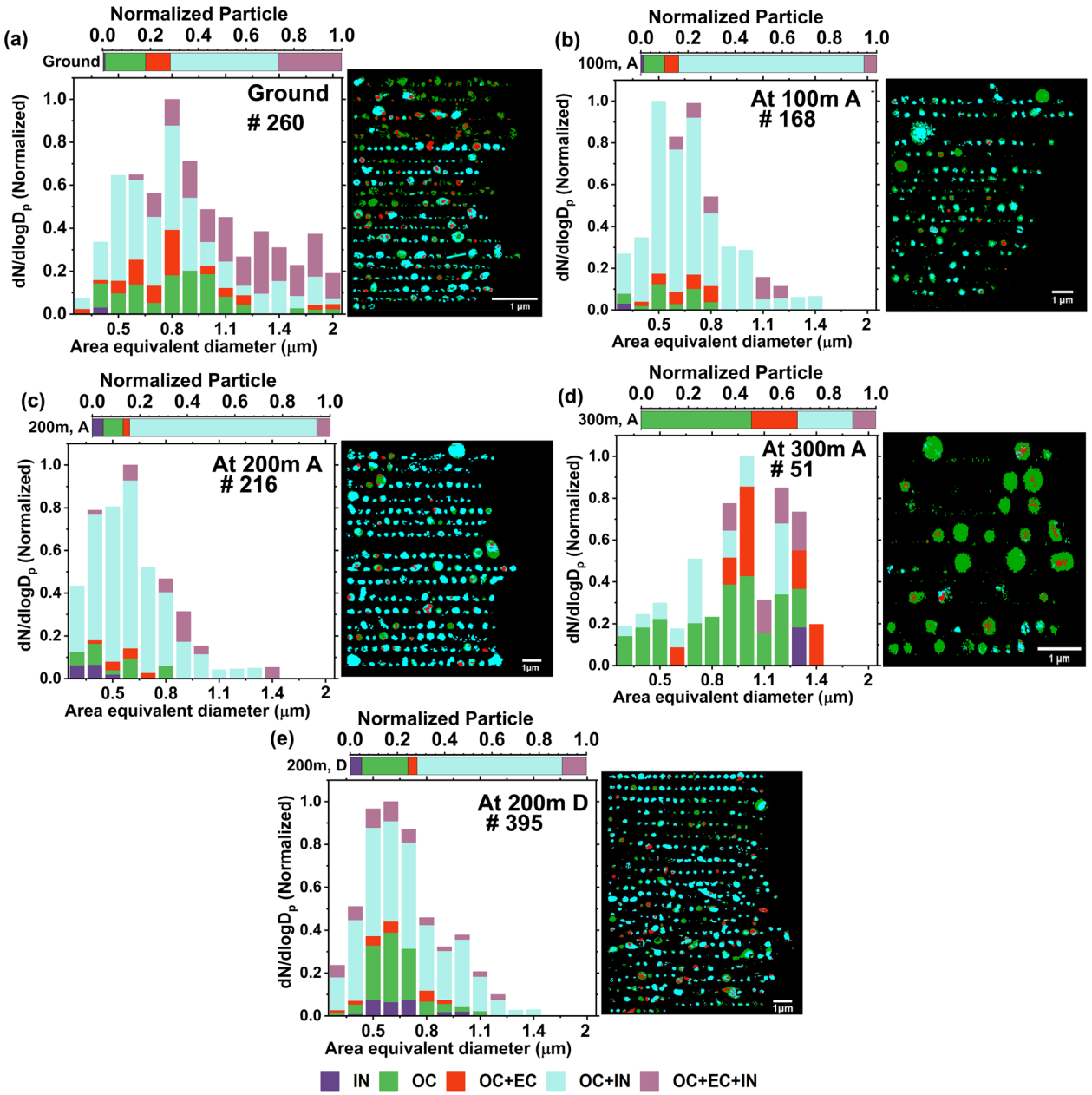

Fig. 3 Chemical mixing state of individual particles collected at different altitudes. (a–e) Distribution of analyzed particles measured by STXM/NEXAFS from ground to different altitudes. To the left of each size-distribution plot, carbon speciation maps are shown. Colors correspond to experimentally defined chemical components; green – organics (OC), red – elemental carbon (EC), and teal – inorganics (IN). Note that each pixel can contain up to three components resulting in overlapping colors. On top of the size-distribution plots, fractions of different classes of internally mixed particles at different times and altitudes are shown. The (#) number inside each plot (a–e) indicate the total number of particles analyzed for each of the samples.

see the presence of different carbon functionalities, including a sharp C=C peak, COOH functional groups, and broad C–OH functionality.

We also retrieved the organic volume fraction (OVF) of the particles from STXM/NEXAFS measurements (Fig. 4). To compare the OVF for all the samples, we categorized OVF into five bins: OVF < 20%, 20 < OVF < 40%, 40 < OVF < 60%, 60 < OVF < 80% and 80 < OVF < 100% as a function of area equivalent diameter. From the OVF measurements, we can see that samples collected at ground level and during 200 m ascending and 200 m descending flights contain high number fractions of low OVF (OVF < 20% and 20–40%) containing particles (79 ± 3% to 70 ± 2%). Particles collected at 100 m altitude are composed of 51 ± 38% low OVF (OVF < 20% and 20–40%), 26 ± 3% moderate OVF (OVF: 40–60%), and 23 ± 3% high OVF (OVF: 60–80% and 80–100%) containing particles. In contrast, particles in samples collected at 300 m are composed of 67 ± 7%, by number, of high OVF (OVF: 60–80% and 80–100%), 18 ± 5%

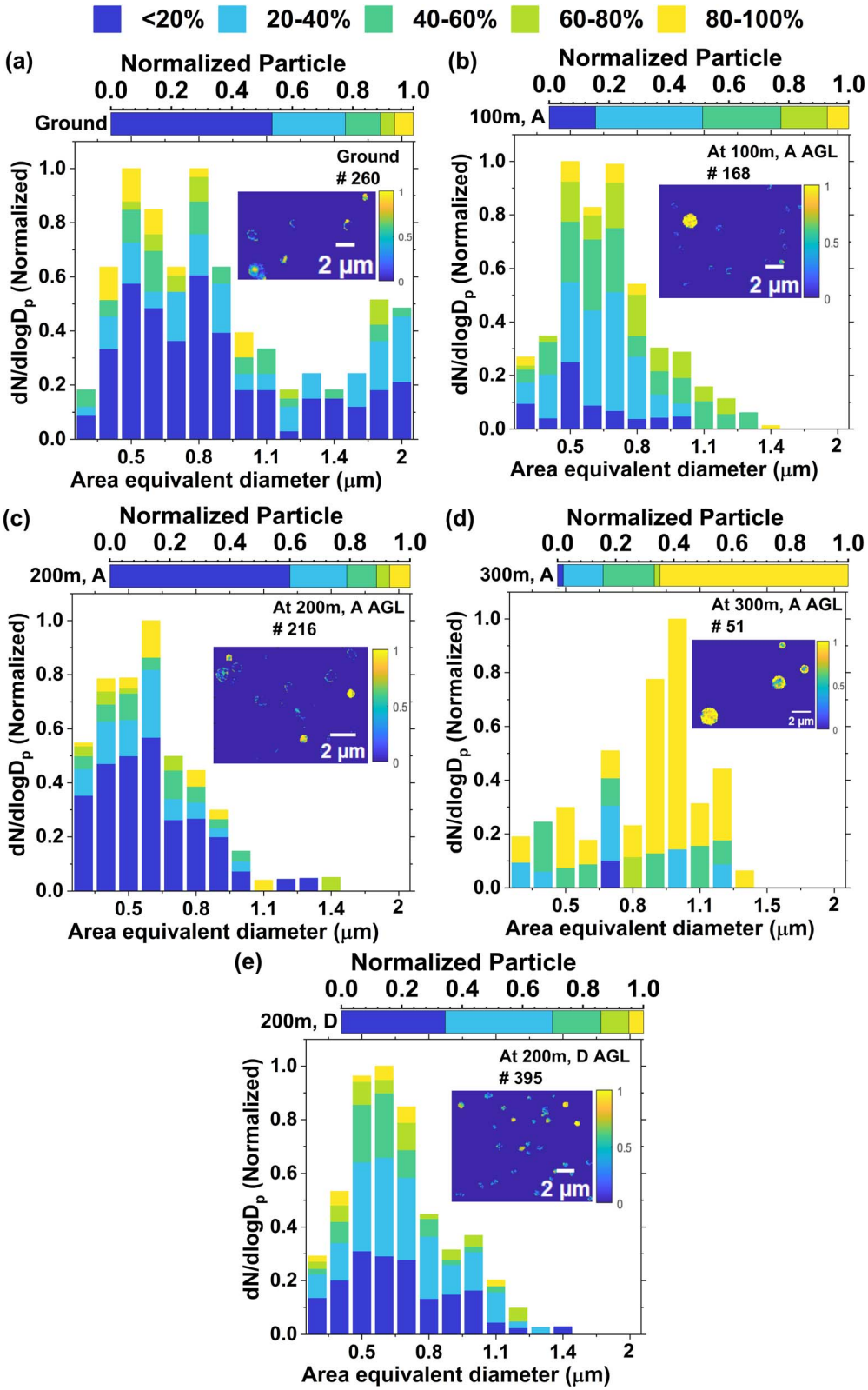

Fig. 4 Organic volume fractions of individual particles collected at different altitudes. (a–e) Distribution of analyzed particles measured by STXM/NEXAFS from ground to different altitudes. Inset of each size-distribution plot, a representative OVF map is shown. On top of the size-distribution plots, fractions of different OVF containing particles at different times and altitudes are shown. The number (#) inside each plot indicates the total number of particles analyzed for each of the samples.

moderate OVF, and 16 ± 5% low OVF-containing particles. We can link the OVF observations with CCSEM/EDX derived particle classes. Particles with low OVF (<20%) are indicating the appearance by inorganic components (IN) likely of dust, Na-rich particles. The moderate OVF (OVF: 20–60%) containing particles are likely to be composed of Na-rich sulfate (aged sea salt), carbonaceous rich sulfate, carbonaceous rich dust, and sulfate rich dust. The particles with high OVF (OVF > 60%) are likely to be composed of carbonaceous-rich particles.

These results indicate that the OVF of the measured particles varied with altitude and may have contributed to the observed differences in particle phase state at different altitudes. A previous study reported that organic aerosol may exist as highly viscous semi-solids or amorphous glassy solids, with implications for atmospheric chemistry, climate, and air quality.[1] Not all organic materials are equally viscous. Some organic components found in aerosols, such as high molecular weight hydrocarbons, can be very viscous, while others, like low molecular weight organic acids, are less so.[91] Therefore, the specific types of organic compounds present in the particle will influence the overall viscosity. Ambient aerosols are complex mixtures, and interactions between organic and inorganic components also can affect viscosity.[1] Water often acts as a plasticizer, reducing the viscosity of organic aerosol particles, while inorganic components can influence the hygroscopicity and phase behavior of these particles, indirectly impacting their viscosity.[1,92] Previous research has indicated that the viscosity of a homogeneous internally mixed particle, which consists of a mixture of organic and inorganic components (such as nitrate, sulfate, and sodium salt), tends to decrease as the proportion of inorganic content goes up.[6,79–84] This decrease in viscosity can be attributed to the greater hygroscopic nature of the inorganic components, resulting in an overall increase in the hygroscopicity of the internally mixed particles. The presence of low inorganic constituents (Na-rich particles, Na-rich sulfate rich particles) possibly explains why we see more high viscosity particles in the case of high OVF-containing sample collected at 300 m.

Additionally, only a limited number of field studies have explored the impact of inorganic inclusions on the viscosity and/or phase state of ambient organic aerosol particles.[19,54] Interestingly, these field studies yielded results consistent with laboratory findings.[19,54] One study observed lower viscosity and increased liquid state during the daytime, which were attributed to higher inorganic sulfate levels,[54] and another study reported a significant abundance of liquid-state particles in Shenzhen, China, associated with elevated inorganic mass fractions in the particles.[19] Hence, our findings are corroborated by both laboratory and field studies, as the ground sample and sample collected at 200 m (ascending and descending) contain abundant inorganic species such as Na-rich and sulfate. The chemical composition associated with these species aligns with the observed trends in the studies. Contrarily, sulfate-lean (sulfate concentration <5%) samples (particles collected at 100 m and 300 m) have more carbonaceous particles and are richer in solid-like particles (28–42%).

4 Conclusion

In this study, we compared the chemical compositions and phase states of individual submicron-size particles collected at ground level and aloft at three altitudes above an Alaskan Arctic oil field. Our findings reveal that most of these particles are considerably influenced by local anthropogenic emissions, such as those from oil field activities and combustion processes. Our results are consistent with previous studies, conducted on the North Slope of Alaska, which have also reported the presence of complex aerosol mixtures influenced by both natural and anthropogenic sources.[36,38,40,41,43,44] These studies highlight the significant role of anthropogenic activities, particularly oil extraction and combustion processes, in shaping the chemical and physical properties of Arctic aerosols.

Understanding the phase states of particles at different altitudes will aid in predicting and modeling ice crystal growth, cloud formation, and subsequent impacts on Earth's climate.[7] Our results indicate that particles collected at 300 m above ground level were comprised of organic-rich constituents with high viscosities, suggesting these particles may promote ice formation under cirrus cloud condition if they are transported to higher altitudes.[10,93] Although these particles were initially observed near the ground surface, atmospheric dynamics can lead to their vertical transport, making their phase state and composition relevant for ice nucleation processes at higher altitudes. Particle sample collected above ground is composed of less organic-rich, more organic-mixed with inorganic rich and relatively less high viscosity particles than at 300 m above aground level.

Additionally, the knowledge gained from this study can have implications for the diffusion time scale and secondary organic aerosol (SOA) partitioning.[94,95] Although direct SOA and diffusion measurements were not performed, the observed chemical compositions and phase states offer indirect insights into these processes. For instance, the internal mixing of sulfur with carbonaceous particles observed in our study suggests contributions from secondary sulfate production. Sulfur compounds, such as sulfates, contribute to changes in the overall particle phase state, making them more hygroscopic and likely to decrease the viscosity of the entire particle. This decreased viscosity may reduce diffusion time scales within the particle, thereby facilitating the partitioning of organic vapors, which is a critical aspect of SOA formation. Moreover, the increased hygroscopicity and decreased viscosity can enhance the chemical reactivity of the particles, thus facilitating heterogeneous reactions.[96] In this study, we observed samples containing high sulfate-rich particles with a higher fraction of low-viscosity particles. A more comprehensive understanding of phase state variations at different altitudes can improve our understanding of atmospheric mixing and transport processes, as these phase characteristics are known to influence both SOA partitioning and diffusion timescales.

Despite the valuable insights gained, our study has certain limitations that warrant consideration. Our research provides insight into the early winter aerosol phase state above an Arctic

oil field, highlighting specific conditions and behaviors unique to this period and location. This is important in the context of increasing development and resource extraction in the Arctic[97] and other regions of the Arctic with similar oil fields.[85,98] However, this focus on a single case day may not represent the complexities of the Arctic atmosphere under different atmospheric conditions. Therefore, caution should be exercised when extrapolating these findings to other areas. Additionally, our study was conducted during specific atmospheric conditions of Arctic wintertime, and we would expect significant differences across different seasons. Further research should be conducted under a range of boundary layer turbulence conditions from well mixed to stratified, and across a range of temperatures, to provide a more comprehensive understanding of particle phase state variations under diverse scenarios. The analytical framework developed here offers an approach for studying individual aerosol phase states in various climatic and geographic contexts. Despite the limitations of this study, it provides valuable insights into the vertical variability of the phase state of individual particles and their association with chemical composition. Finally, this research underscores the importance of studying aerosol particles from oil fields due to their increasing impact on the Arctic environment,[85] particularly concerning cloud properties[37] and climate predictions.

Data availability

Data are reported in tabular form in the ESI.† *In situ* aerosol and meteorological measurements data used in this study are available in ARM data archive (DOI: **https://doi.org/10.5439/1352536**, **https://doi.org/10.5439/1827703**).

Conflicts of interest

The authors declare no conflicts of interest relevant to this study.

Acknowledgements

Some of this research was funded using project awards (10.46936/prtn.proj.2020.51252/60000164 and 10.46936/lser.proj.2020.51377/60000185), using resources at the Environmental Molecular Sciences Laboratory (EMSL) and the Atmospheric Radiation Measurement facility (ARM), which are U.S. Department of Energy (DOE) Scientific User Facilities. Both facilities are sponsored by the Office of Biological and Environmental Research (OBER) and operated under Contract No. DE-AC05-76RL01830 (EMSL) and DE-FG03-00ER62913 and DE-FG03-97ER62338 (ARM). K. A. Pratt acknowledges support from a DOE Early Career Award (DE-SC0019172). Online aerosol measurement, meteorological datasets were obtained from the ARM Program sponsored by the OBER Climate and Environmental Sciences Division. STXM/NEXAFS analysis at beamline 5.3.2.2 of the Advanced Light Source at Lawrence Berkeley National Laboratory is supported by the Director, DOE Office of Science, Office of Basic Energy Sciences under Contract No. DE-AC02-05CH11231.

References

1 J. P. Reid, A. K. Bertram, D. O. Topping, A. Laskin, S. T. Martin, M. D. Petters, F. D. Pope and G. Rovelli, *Nat. Commun.*, 2018, **9**, 956.
2 N. Bellouin, J. Quaas, E. Gryspeerdt, S. Kinne, P. Stier, D. Watson-Parris, O. Boucher, K. S. Carslaw, M. Christensen, A.-L. Daniau, J.-L. Dufresne, G. Feingold, S. Fiedler, P. Forster, A. Gettelman, J. M. Haywood, U. Lohmann, F. Malavelle, T. Mauritsen, D. T. McCoy, G. Myhre, J. Mülmenstädt, D. Neubauer, A. Possner, M. Rugenstein, Y. Sato, M. Schulz, S. E. Schwartz, O. Sourdeval, T. Storelvmo, V. Toll, D. Winker and B. Stevens, *Rev. Geophys.*, 2020, **58**, e2019RG000660.
3 S. M. Burrows, C. S. McCluskey, G. Cornwell, I. Steinke, K. Zhang, B. Zhao, M. Zawadowicz, A. Raman, G. Kulkarni, S. China, A. Zelenyuk and P. J. DeMott, *Rev. Geophys.*, 2022, **60**, e2021RG000745.
4 K. Ignatius, T. B. Kristensen, E. Järvinen, L. Nichman, C. Fuchs, H. Gordon, P. Herenz, C. R. Hoyle, J. Duplissy, S. Garimella, A. Dias, C. Frege, N. Höppel, J. Tröstl, R. Wagner, C. Yan, A. Amorim, U. Baltensperger, J. Curtius, N. M. Donahue, M. W. Gallagher, J. Kirkby, M. Kulmala, O. Möhler, H. Saathoff, M. Schnaiter, A. Tomé, A. Virtanen, D. Worsnop and F. Stratmann, *Atmos. Chem. Phys.*, 2016, **16**, 6495–6509.
5 K. J. Baustian, M. E. Wise, E. J. Jensen, G. P. Schill, M. A. Freedman and M. A. Tolbert, *Atmos. Chem. Phys.*, 2013, **13**, 5615–5628.
6 G. P. Schill, D. O. De Haan and M. A. Tolbert, *Environ. Sci. Technol.*, 2014, **48**, 1675–1682.
7 D. A. Knopf, P. A. Alpert and B. Wang, *ACS Earth Space Chem.*, 2018, **2**, 168–202.
8 N. N. Lata, B. Zhang, S. Schum, L. Mazzoleni, R. Brimberry, M. A. Marcus, W. H. Cantrell, P. Fialho, C. Mazzoleni and S. China, *ACS Earth Space Chem.*, 2021, **5**, 3499–3510.
9 T. Berkemeier, M. Shiraiwa, U. Pöschl and T. Koop, *Atmos. Chem. Phys.*, 2014, **14**, 12513–12531.
10 B. J. Murray, T. W. Wilson, S. Dobbie, Z. Cui, S. M. R. K. Al-Jumur, O. Möhler, M. Schnaiter, R. Wagner, S. Benz, M. Niemand, H. Saathoff, V. Ebert, S. Wagner and B. Kärcher, *Nat. Geosci.*, 2010, **3**, 233–237.
11 W. Tan, C. Li, Y. Liu, X. Meng, Z. Wu, L. Kang and T. Zhu, *Environ. Sci. Technol. Lett.*, 2020, **7**, 54–59.
12 U. Pöschl and M. Shiraiwa, *Chem. Rev.*, 2015, **115**, 4440–4475.
13 L. Renbaum-Wolff, J. W. Grayson, A. P. Bateman, M. Kuwata, M. Sellier, B. J. Murray, J. E. Shilling, S. T. Martin and A. K. Bertram, *Proc. Natl. Acad. Sci. U. S. A.*, 2013, **110**, 8014–8019.
14 M. Shrivastava, S. Lou, A. Zelenyuk, R. C. Easter, R. A. Corley, B. D. Thrall, P. J. Rasch, J. D. Fast, S. L. Massey Simonich, H. Shen and S. Tao, *Proc. Natl. Acad. Sci. U. S. A.*, 2017, **114**, 1246–1251.
15 A. Zelenyuk, D. Imre, J. Beránek, E. Abramson, J. Wilson and M. Shrivastava, *Environ. Sci. Technol.*, 2012, **46**, 12459–12466.

16 M. Shiraiwa and J. H. Seinfeld, *Geophys. Res. Lett.*, 2012, **39**, L24801.
17 T. Koop, J. Bookhold, M. Shiraiwa and U. Pöschl, *Phys. Chem. Chem. Phys.*, 2011, **13**, 19238–19255.
18 M. Shiraiwa, Y. Li, A. P. Tsimpidi, V. A. Karydis, T. Berkemeier, S. N. Pandis, J. Lelieveld, T. Koop and U. Pöschl, *Nat. Commun.*, 2017, **8**, 15002.
19 Y. Liu, Z. Wu, X. Huang, H. Shen, Y. Bai, K. Qiao, X. Meng, W. Hu, M. Tang and L. He, *Environ. Sci. Technol.*, 2019, **53**, 5027–5033.
20 S. R. Schill, D. B. Collins, C. Lee, H. S. Morris, G. A. Novak, K. A. Prather, P. K. Quinn, C. M. Sultana, A. V. Tivanski, K. Zimmermann, C. D. Cappa and T. H. Bertram, *ACS Cent. Sci.*, 2015, **1**, 132–141.
21 C. P. Kaluarachchi, V. W. Or, Y. Lan, C. K. Madawala, E. S. Hasenecz, D. R. Crocker, C. K. Morris, H. D. Lee, K. J. Mayer, J. S. Sauer, C. Lee, G. Dorce, F. Malfatti, E. A. Stone, C. D. Cappa, V. H. Grassian, K. A. Prather and A. V. Tivanski, *ACS Earth Space Chem.*, 2022, **6**, 116–130.
22 S. T. Martin, *Chem. Rev.*, 2000, **100**, 3403–3454.
23 C. Marcolli, B. Luo and T. Peter, *J. Phys. Chem. A*, 2004, **108**, 2216–2224.
24 M. Shrivastava, C. D. Cappa, J. Fan, A. H. Goldstein, A. B. Guenther, J. L. Jimenez, C. Kuang, A. Laskin, S. T. Martin, N. L. Ng, T. Petaja, J. R. Pierce, P. J. Rasch, P. Roldin, J. H. Seinfeld, J. Shilling, J. N. Smith, J. A. Thornton, R. Volkamer, J. Wang, D. R. Worsnop, R. A. Zaveri, A. Zelenyuk and Q. Zhang, *Rev. Geophys.*, 2017, **55**, 509–559.
25 J. L. Jimenez, M. R. Canagaratna, N. M. Donahue, A. S. H. Prevot, Q. Zhang, J. H. Kroll, P. F. DeCarlo, J. D. Allan, H. Coe, N. L. Ng, A. C. Aiken, K. S. Docherty, I. M. Ulbrich, A. P. Grieshop, A. L. Robinson, J. Duplissy, J. D. Smith, K. R. Wilson, V. A. Lanz, C. Hueglin, Y. L. Sun, J. Tian, A. Laaksonen, T. Raatikainen, J. Rautiainen, P. Vaattovaara, M. Ehn, M. Kulmala, J. M. Tomlinson, D. R. Collins, M. J. Cubison, E. J. Dunlea, J. A. Huffman, T. B. Onasch, M. R. Alfarra, P. I. Williams, K. Bower, Y. Kondo, J. Schneider, F. Drewnick, S. Borrmann, S. Weimer, K. Demerjian, D. Salcedo, L. Cottrell, R. Griffin, A. Takami, T. Miyoshi, S. Hatakeyama, A. Shimono, J. Y. Sun, Y. M. Zhang, K. Dzepina, J. R. Kimmel, D. Sueper, J. T. Jayne, S. C. Herndon, A. M. Trimborn, L. R. Williams, E. C. Wood, A. M. Middlebrook, C. E. Kolb, U. Baltensperger and D. R. Worsnop, *Science*, 2009, **326**, 1525–1529.
26 P. Tunved, J. Ström and R. Krejci, *Atmos. Chem. Phys.*, 2013, **13**, 3643–3660.
27 D. Zhang, J. Comstock, H. Xie and Z. Wang, *Remote Sens.*, 2022, **14**, 4638.
28 K. S. Law and A. Stohl, *Science*, 2007, **315**, 1537–1540.
29 K. S. Law, A. Stohl, P. K. Quinn, C. A. Brock, J. F. Burkhart, J.-D. Paris, G. Ancellet, H. B. Singh, A. Roiger, H. Schlager, J. Dibb, D. J. Jacob, S. R. Arnold, J. Pelon and J. L. Thomas, *Bull. Am. Meteorol. Soc.*, 2014, **95**, 1873–1895.
30 R. S. Stone, S. Sharma, A. Herber, K. Eleftheriadis and D. W. Nelson, *Elem. Sci. Anth.*, 2014, **2**, 000027.
31 P. K. Quinn, T. L. Miller, T. S. Bates, J. A. Ogren, E. Andrews and G. E. Shaw, *J. Geophys. Res.:Atmos.*, 2002, **107**, 1–15.
32 P. K. Quinn, G. Shaw, E. Andrews, E. G. Dutton, T. Ruoho-Airola and S. L. Gong, *Tellus B*, 2007, **59**, 99–114.
33 M. D. Willis, W. R. Leaitch and J. P. D. Abbatt, *Rev. Geophys.*, 2018, **56**, 621–671.
34 D. Desilets, F. M. Helsel, A. O. Bendure, D. A. Lucero, M. D. Ivey and D. N. Dexheimer, *Visitor's Guide to Oliktok Point Atmospheric Radiation Measurement Climate Research Facility, North Slope of Alaska, DOE ARM Climate Research Facility*, Pacific Northwest National Laboratory, Richland, WA, 2016.
35 G. de Boer, D. Dexheimer, F. Mei, J. Hubbe, C. Longbottom, P. J. Carroll, M. Apple, L. Goldberger, D. Oaks, J. Lapierre, M. Crume, N. Bernard, M. D. Shupe, A. Solomon, J. Intrieri, D. Lawrence, A. Doddi, D. J. Holdridge, M. Hubbell, M. D. Ivey and B. Schmid, *Earth Syst. Sci. Data*, 2019, **11**, 1349–1362.
36 J. M. Creamean, M. Maahn, G. de Boer, A. McComiskey, A. J. Sedlacek and Y. Feng, *Atmos. Chem. Phys.*, 2018, **18**, 555–570.
37 M. Maahn, G. de Boer, J. M. Creamean, G. Feingold, G. M. McFarquhar, W. Wu and F. Mei, *Atmos. Chem. Phys.*, 2017, **17**, 14709–14726.
38 M. J. Gunsch, R. M. Kirpes, K. R. Kolesar, T. E. Barrett, S. China, R. J. Sheesley, A. Laskin, A. Wiedensohler, T. Tuch and K. A. Pratt, *Atmos. Chem. Phys.*, 2017, **17**, 10879–10892.
39 J. M. Creamean, R. M. Kirpes, K. A. Pratt, N. J. Spada, M. Maahn, G. de Boer, R. C. Schnell and S. China, *Atmos. Chem. Phys.*, 2018, **18**, 18023–18042.
40 R. M. Kirpes, A. L. Bondy, D. Bonanno, R. C. Moffet, B. Wang, A. Laskin, A. P. Ault and K. A. Pratt, *Atmos. Chem. Phys.*, 2018, **18**, 3937–3949.
41 J. Liu, M. J. Gunsch, C. E. Moffett, L. Xu, R. El Asmar, Q. Zhang, T. B. Watson, H. M. Allen, J. D. Crounse, J. St. Clair, M. Kim, P. O. Wennberg, R. J. Weber, R. J. Sheesley and K. A. Pratt, *Environ. Sci. Technol. Lett.*, 2021, **8**, 511–518.
42 C. E. Moffett, T. E. Barrett, J. Liu, M. J. Gunsch, L. M. Upchurch, P. K. Quinn, K. A. Pratt and R. J. Sheesley, *J. Geophys. Res.:Atmos.*, 2020, **125**, e2020JD033225.
43 C. E. Moffett, M. Mehra, T. E. Barrett, M. J. Gunsch, K. A. Pratt and R. J. Sheesley, *Sci. Total Environ.*, 2022, **831**, 154641.
44 M. J. Gunsch, J. Liu, C. E. Moffett, R. J. Sheesley, N. Wang, Q. Zhang, T. B. Watson and K. A. Pratt, *Environ. Sci. Technol.*, 2020, **54**, 92–101.
45 A. P. Bateman, H. Belassein and S. T. Martin, *Aerosol Sci. Technol.*, 2014, **48**, 42–52.
46 A. P. Bateman, A. K. Bertram and S. T. Martin, *J. Phys. Chem. A*, 2015, **119**, 4386–4395.
47 N. A. Hosny, C. Fitzgerald, A. Vyšniauskas, A. Athanasiadis, T. Berkemeier, N. Uygur, U. Pöschl, M. Shiraiwa, M. Kalberer, F. D. Pope and M. K. Kuimova, *Chem. Sci.*, 2016, **7**, 1357–1367.

48 S. Jain and G. A. Petrucci, *Aerosol Sci. Technol.*, 2015, **49**, 390–399.
49 A. Pajunoja, W. Hu, Y. J. Leong, N. F. Taylor, P. Miettinen, B. B. Palm, S. Mikkonen, D. R. Collins, J. L. Jimenez and A. Virtanen, *Atmos. Chem. Phys.*, 2016, **16**, 11163–11176.
50 Y.-J. Li, P.-F. Liu, C. Bergoend, A. P. Bateman and S. T. Martin, *Aerosol Sci. Technol.*, 2017, **51**, 388–396.
51 A. Virtanen, J. Joutsensaari, T. Koop, J. Kannosto, P. Yli-Pirilä, J. Leskinen, J. M. Mäkelä, J. K. Holopainen, U. Pöschl, M. Kulmala, D. R. Worsnop and A. Laaksonen, *Nature*, 2010, **467**, 824–827.
52 A. P. Bateman, Z. Gong, P. Liu, B. Sato, G. Cirino, Y. Zhang, P. Artaxo, A. K. Bertram, A. O. Manzi, L. V. Rizzo, R. A. F. Souza, R. A. Zaveri and S. T. Martin, *Nat. Geosci.*, 2016, **9**, 34–37.
53 A. P. Bateman, Z. Gong, T. H. Harder, S. S. de Sá, B. Wang, P. Castillo, S. China, Y. Liu, R. E. O'Brien, B. B. Palm, H.-W. Shiu, G. G. Cirino, R. Thalman, K. Adachi, M. L. Alexander, P. Artaxo, A. K. Bertram, P. R. Buseck, M. K. Gilles, J. L. Jimenez, A. Laskin, A. O. Manzi, A. Sedlacek, R. A. F. Souza, J. Wang, R. Zaveri and S. T. Martin, *Atmos. Chem. Phys.*, 2017, **17**, 1759–1773.
54 J. H. Slade, A. P. Ault, A. T. Bui, J. C. Ditto, Z. Lei, A. L. Bondy, N. E. Olson, R. D. Cook, S. J. Desrochers, R. M. Harvey, M. H. Erickson, H. W. Wallace, S. L. Alvarez, J. H. Flynn, B. E. Boor, G. A. Petrucci, D. R. Gentner, R. J. Griffin and P. B. Shepson, *Environ. Sci. Technol.*, 2019, **53**, 4977–4987.
55 R. M. Kirpes, Z. Lei, M. Fraund, M. J. Gunsch, N. W. May, T. E. Barrett, C. E. Moffett, A. J. Schauer, B. Alexander, L. M. Upchurch, S. China, P. K. Quinn, R. C. Moffet, A. Laskin, R. J. Sheesley, K. A. Pratt and A. P. Ault, *Proc. Natl. Acad. Sci. U. S. A.*, 2022, **119**, e2104496119.
56 Z. Cheng, N. Sharma, K.-P. Tseng, L. Kovarik and S. China, *RSC Adv.*, 2021, **11**, 15264–15272.
57 M. Song, R. Jeong, D. Kim, Y. Qiu, X. Meng, Z. Wu, A. Zuend, Y. Ha, C. Kim, H. Kim, S. Gaikwad, K.-S. Jang, J. Y. Lee and J. Ahn, *Environ. Sci. Technol.*, 2022, **56**, 17581–17590.
58 Z. Cheng, M. Morgenstern, B. Zhang, M. Fraund, N. N. Lata, R. Brimberry, M. A. Marcus, L. Mazzoleni, P. Fialho, S. Henning, B. Wehner, C. Mazzoleni and S. China, *Atmos. Chem. Phys.*, 2022, **22**, 9033–9057.
59 W. Li, L. Liu, J. Zhang, L. Xu, Y. Wang, Y. Sun and Z. Shi, *Environ. Sci. Technol.*, 2021, **55**, 2234–2242.
60 N. N. Lata, Z. Cheng, D. Dexheimer, D. Zhang, F. Mei and S. China, *Environ. Sci. Technol.*, 2023, **57**, 5821–5830.
61 Y. Li, A. G. Carlton and M. Shiraiwa, *ACS Earth Space Chem.*, 2021, **5**, 1971–1982.
62 Q. Z. Rasool, M. Shrivastava, M. Octaviani, B. Zhao, B. Gaudet and Y. Liu, *ACS Earth Space Chem.*, 2021, **5**, 2910–2924.
63 B. Wang, T. H. Harder, S. T. Kelly, D. S. Piens, S. China, L. Kovarik, M. Keiluweit, B. W. Arey, M. K. Gilles and A. Laskin, *Nat. Geosci.*, 2016, **9**, 433–437.
64 Z. Cheng, A. Liyu, D. Dexheimer, N. Nahar Lata, G. Kulkarni, C. Michael Longbottom, F. Mei and S. China, *Environ. Sci.: Atmos.*, 2022, **2**, 1263–1276.
65 O. Laskina, H. S. Morris, J. R. Grandquist, A. D. Estillore, E. A. Stone, V. H. Grassian and A. V. Tivanski, *Environ. Sci. Technol.*, 2015, **49**, 13447–13453.
66 E. Cromwell, D. Dexheimer, Y. Shi and G. Whitson, *tbsimet.a1, Oak Ridge National Laboratory (ORNL), Atmospheric Radiation Measurement (ARM) Data Center*, Oak Ridge, TN, USA, 2017.
67 F. Mei, G. McMeeking, M. Pekour, R.-S. Gao, G. Kulkarni, S. China, H. Telg, D. Dexheimer, J. Tomlinson and B. Schmid, *Sensors*, 2020, **20**, 6294.
68 A. Laskin, J. P. Cowin and M. J. Iedema, *J. Electron Spectrosc. Relat. Phenom.*, 2006, **150**, 260–274.
69 A. Laskin, *Fundamentals and Applications in Aerosol Spectroscopy*, 2010, p. 463.
70 S. China, B. Scarnato, R. C. Owen, B. Zhang, M. T. Ampadu, S. Kumar, K. Dzepina, M. P. Dziobak, P. Fialho, J. A. Perlinger, J. Hueber, D. Helmig, L. R. Mazzoleni and C. Mazzoleni, *Geophys. Res. Lett.*, 2015, **42**, 1243–1250.
71 R. C. Moffet, T. Henn, A. Laskin and M. K. Gilles, *Anal. Chem.*, 2010, **82**, 7906–7914.
72 R. C. Moffet, A. V. Tivanski and M. K. Gilles, Scanning Transmission X-ray Microscopy, in *Fundamentals and Applications in Aerosol Spectroscopy*, ed. R. Signorell and J. P. Reid, 2010, pp. 243–272.
73 T. J. Collins, *BioTechniques*, 2007, **43**, S25–S30.
74 Modeling results from the HYSPLIT atmospheric transport and dispersion model, **https://www.ready.noaa.gov/hysplit_metadata.html**, accessed 25 January 2024.
75 M. Tjernström and R. G. Graversen, *Q. J. R. Metereol. Soc.*, 2009, **135**, 431–443.
76 Q. Coopman, T. J. Garrett, J. Riedi, S. Eckhardt and A. Stohl, *Atmos. Chem. Phys.*, 2016, **16**, 4661–4674.
77 M. A. Thomas, A. Devasthale, M. Tjernström and A. M. L. Ekman, *Geophys. Res. Lett.*, 2019, **46**, 2836–2845.
78 O. M. Almethen and Z. S. Aldaithan, *Indian J. Environ. Sci.*, 2017, **6**, 74–79.
79 H. P. Dette and T. Koop, *J. Phys. Chem. A*, 2015, **119**, 4552–4561.
80 R. M. Power, S. H. Simpson, J. P. Reid and A. J. Hudson, *Chem. Sci.*, 2013, **4**, 2597–2604.
81 G. Rovelli, Y.-C. Song, A. M. Maclean, D. O. Topping, A. K. Bertram and J. P. Reid, *Anal. Chem.*, 2019, **91**, 5074–5082.
82 E. Saukko, A. T. Lambe, P. Massoli, T. Koop, J. P. Wright, D. R. Croasdale, D. A. Pedernera, T. B. Onasch, A. Laaksonen, P. Davidovits, D. R. Worsnop and A. Virtanen, *Atmos. Chem. Phys.*, 2012, **12**, 7517–7529.
83 Y.-C. Song, J. Lilek, J. B. Lee, M. N. Chan, Z. Wu, A. Zuend and M. Song, *Atmos. Chem. Phys.*, 2021, **21**, 10215–10228.
84 B. Wang, R. E. O'Brien, S. T. Kelly, J. E. Shilling, R. C. Moffet, M. K. Gilles and A. Laskin, *J. Phys. Chem. A*, 2015, **119**, 4498–4508.
85 G. P. Peters, T. B. Nilssen, L. Lindholt, M. S. Eide, S. Glomsrød, L. I. Eide and J. S. Fuglestvedt, *Atmos. Chem. Phys.*, 2011, **11**, 5305–5320.
86 A. V. Tivanski, R. J. Hopkins, T. Tyliszczak and M. K. Gilles, *J. Phys. Chem. A*, 2007, **111**, 5448–5458.

87 K. Adachi and P. R. Buseck, *J. Geophys. Res.:Atmos.*, 2011, **116**, D5.
88 D. L. Bones, J. P. Reid, D. M. Lienhard and U. K. Krieger, *Proc. Natl. Acad. Sci. U.S.A.*, 2012, **109**, 11613–11618.
89 B. J. Murray, *Atmos. Chem. Phys. Discuss.*, 2008, **8**, 8743–8771.
90 B. Zobrist, C. Marcolli, D. A. Pedernera and T. Koop, *Atmos. Chem. Phys.*, 2008, **8**, 5221–5244.
91 N. E. Rothfuss and M. D. Petters, *Environ. Sci. Technol.*, 2017, **51**, 271–279.
92 W.-S. W. DeRieux, Y. Li, P. Lin, J. Laskin, A. Laskin, A. K. Bertram, S. A. Nizkorodov and M. Shiraiwa, *Atmos. Chem. Phys.*, 2018, **18**, 6331–6351.
93 R. Wagner, H. Saathoff, M. Schnaiter, J. Skrotzki, T. Leisner, T. W. Wilson, T. L. Malkin and B. J. Murray, *Atmos. Chem. Phys.*, 2012, **12**, 8589.
94 M. Schervish and M. Shiraiwa, *Atmos. Chem. Phys.*, 2023, **23**, 221–233.
95 R. A. Zaveri, J. E. Shilling, A. Zelenyuk, M. A. Zawadowicz, K. Suski, S. China, D. M. Bell, D. Veghte and A. Laskin, *Environ. Sci. Technol.*, 2020, **54**, 2595–2605.
96 Y. J. Li, P. Liu, Z. Gong, Y. Wang, A. P. Bateman, C. Bergoend, A. K. Bertram and S. T. Martin, *Environ. Sci. Technol.*, 2015, **49**, 13264–13274.
97 J. Schmale, S. R. Arnold, K. S. Law, T. Thorp, S. Anenberg, W. R. Simpson, J. Mao and K. A. Pratt, *Earth's Future*, 2018, **6**, 1385–1412.
98 A. Roiger, J. L. Thomas, H. Schlager, K. S. Law, J. Kim, A. Schäfler, B. Weinzierl, F. Dahlkötter, I. Krisch, L. Marelle and A. Minikin, *Bull. Am. Meteorol. Soc.*, 2015, **96**, 441–460.